

Annual Review of Physical Chemistry

The Optical Signatures of Stochastic Processes in Many-Body Exciton Scattering

Hao Li, S.A. Shah, Ajay Ram Srimath Kandada, 2 Carlos Silva,³ Andrei Pirvatinski,⁴ and Eric R. Bittner¹

Annu. Rev. Phys. Chem. 2023. 74:20.1-20.26

The Annual Review of Physical Chemistry is online at physchem.annualreviews.org

https://doi.org/10.1146/annurev-physchem-102822-

Copyright © 2023 by the author(s). All rights reserved

Keywords

excitation-induced dephasing, many-body effects in quantum dynamics, coherent nonlinear spectroscopy, quantum stochastic calculus

Abstract

We review our recent quantum stochastic model for spectroscopic lineshapes in the presence of a coevolving and nonstationary background population of excitations. Starting from a field theory description for interacting bosonic excitons, we derive a reduced model whereby optical excitons are coupled to an incoherent background via scattering as mediated by their screened Coulomb coupling. The Heisenberg equations of motion for the optical excitons are then driven by an auxiliary stochastic population variable, which we take to be the solution of an Ornstein-Uhlenbeck process. Here, we present an overview of the theoretical techniques we have developed as applied to predicting coherent nonlinear spectroscopic signals. We show how direct (Coulomb) and exchange coupling to the bath give rise to distinct spectral signatures and discuss mathematical limits on inverting spectral signatures to extract the background density of states.





¹Department of Chemistry, University of Houston, Houston, Texas, USA; email: ebittner@central.uh.edu

²Department of Physics and Center for Functional Materials, Wake Forest University, Winston-Salem, North Carolina, USA

³School of Chemistry and Biochemistry, School of Physics, and School of Materials Science and Engineering, Georgia Institute of Technology, Atlanta, Georgia, USA

⁴Theoretical Division, Los Alamos National Laboratory, Los Alamos, New Mexico, USA

EID:

1. INTRODUCTION

transition-metal dichalchogenide

excitation-induced

It is well recognized that many-body phenomena have a profound effect on the linear and nonlinear optical lineshapes of semiconductors with reduced dimensionality, in which Coulomb correlations can be particularly strong due to decreased screening and quantum confinement effects. One such effect is biexciton formation, in which Coulomb binding of two electron-hole pairs results in new two-electron, two-hole quasi-particles (1-11). Another important process that is highly relevant in exciton quantum dynamics is excitation-induced dephasing (EID) (12-28), investigated primarily in 2D systems such as III-V quantum wells (13, 18-20, 22-24), singlelayer transition-metal dichalchogenides (TMDCs) (25, 26), quantum dot photocells (28), and 2D metal-halide perovskite derivatives (27). This can be described as the incoherent Coulomb elastic scattering between multiple excitons or between excitons and an electron-hole plasma generated with the excitation optical field. The scattering process gives rise to faster dephasing dynamics compared with the low-density pure-dephasing limit and may be the dominant dephasing pathway at sufficiently high densities. In many systems, especially those with strong exciton-phonon coupling, the background excitations are transient and coevolve with optical modes of the system, and consequently a strictly incoherent kinetic description such as this mesoscopic approach or a kinetic Markovian Boltzmann-like scattering theory (15) cannot describe coherence dynamics. EID can be effectively rationalized from a mesoscopic perspective by means of the optical Bloch equations (OBEs), which capture the effect of many-body exciton scattering on both population and coherence dynamics derived from coherent spectroscopy of semiconductors (20, 21).

Recent advances toward a more microscopic perspective have been presented by Katsch et al. (29), who used excitonic Heisenberg equations of motion to describe linear excitation line broadening in 2D TMDCs. Their results indicate exciton-exciton scattering from a dark background as a dominant mechanism in the power-dependent broadening EID and sideband formation. Similar theoretical modeling on this class of materials and their van der Waals bilayers has yielded insight into the role of effective mass asymmetry on EID processes (30). These modeling works highlight the need for microscopic approaches to understand nonlinear quantum dynamics of complex 2D semiconductors, but the computational expense could become considerable if other many-body details such as polaronic effects are to be included (31). As an alternative general approach, we recently developed an analytical theory of dephasing in the same vein as Anderson–Kubo lineshape theory (32, 33) that includes transient EID and Coulomb screening effects, which are valuable for extracting microscopic details about screened exciton-exciton scattering from time-dependent nonlinear coherent ultrafast spectroscopy, via direct and unambiguous measurement of the homogeneous excitation linewidth (34, 35).

Here, we present an overview of our work that employs a quantum stochastic approach, derived from a first-principles many-body theory of interacting excitons, to develop a mostly analytical model that describes linear and nonlinear spectral lineshapes that result from exciton-exciton scattering processes and, importantly, their dependence on population time due to the evolution of a nonstationary/nonequilibrium excitation background (see **Figure 1***a*). Our approach is similar in spirit to the celebrated Anderson–Kubo theory (32, 33) and reduces to that in the limit of a stationary background population at sufficiently long times (36). The model captures a microscopic picture of EID by integrating over the interactions of excitons produced via a well-defined coherent pathway (**Figure 2**). The background excitons that do not have a well-defined phase relationship induced by the optical field can be treated as a nonstationary source of quantum noise. In doing so, we can directly insert the spectral density of the bath into nonlinear spectral response functions and obtain fully analytical expressions for the coherent exciton lineshapes.

We implement the model to investigate the evolution of the 2D coherent excitation lineshape in a polycrystalline thin film of a prototypical 2D single-layer metal-halide perovskite derivative,







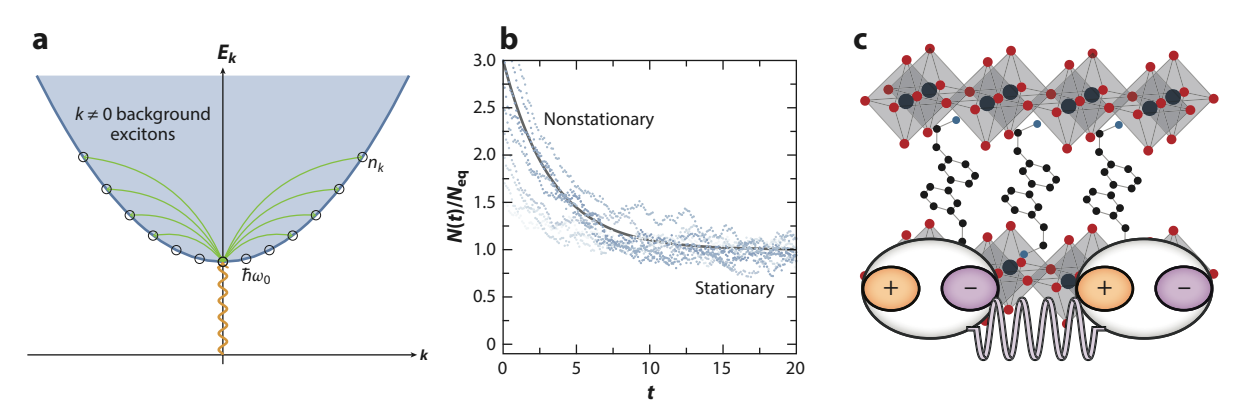


Figure 1

(a) Schematic representation of optical absorption of excitons and exciton-exciton scattering with a background population, in which the dispersion relation is in the exciton representation and $\mathbf{k} = \mathbf{k}_e + \mathbf{k}_b$ is the exciton wave vector. (b) Time evolution of population $N(t)/N_{\rm eq}$ from an initial nonstationary state produced by exciton injection. Individual trajectories are represented by blue dots. Asymptotically, the function reaches a stationary state that yields the Anderson–Kubo limit. (c) Crystal structure of (PEA)₂PbI₄ with a schematic representation of exciton-exciton elastic scattering interactions. Figure adapted with permission from Reference 37; copyright 2020 American Institute of Physics. Abbreviation: (PEA)₂PbI₄, phenylethylammonium lead iodide.

phenylethylammonium lead iodide [(PEA)₂PbI₄] (for the crystal structure, see **Figure 1c**). We have selected this material as a model system because of its well-defined exciton lineshape, which we have modeled quantitatively within a Wannier–Mott framework (38), and because it displays strong many-body phenomena such as strongly bound biexcitons at room temperature (39) and robust EID effects (27). Furthermore, we have concluded that the primary excitations are exciton polarons (31, 40), quasi-particles with Coulomb correlations that are renormalized by lattice

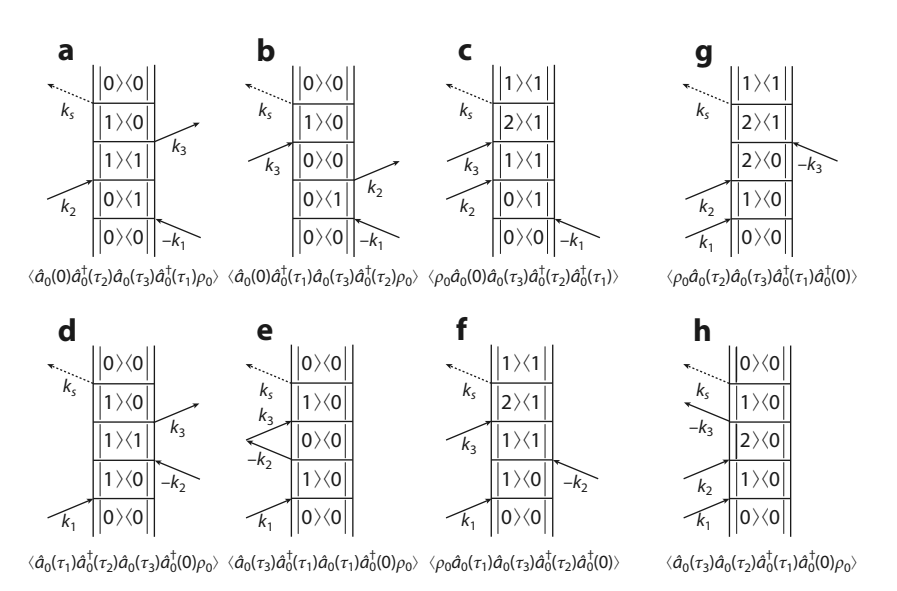


Figure 2

Double-sided Feynman diagrams for coherent response functions (Equation 20) with rephasing phase-matching, (a) R_{2a} , (b) R_{3a} , and (c) R_{1b}^* ; nonrephasing phase-matching, (d) R_{1a} , (e) R_{4a} , and (f) R_{2b}^* ; and double quantum phase-matching, (g) R_{3b}^* and (b) R_{4b} .



Dispersive lineshape: the 2D spectrum has odd reflection symmetry along the off-diagonal axis

Absorptive lineshape: a diagonal slice of a 2D spectrum directly maps onto the linear absorption spectra of the system and has even reflection symmetry along the off-diagonal axis

Rephasing: $\mathbf{k}_s = -\mathbf{k}_1 + \mathbf{k}_2 + \mathbf{k}_3$

Nonrephasing: $\mathbf{k}_s = \mathbf{k}_1 - \mathbf{k}_2 + \mathbf{k}_3$

EIS: excitation-induced shift

dynamics via polaronic effects; both electron-hole and photocarrier-lattice correlations are ingredients of the system Hamiltonian, such that the lattice dressing constitutes an integral component of its eigenstates and eigenvalues. This renders the system in a highly dynamically disordered state, such that lattice screening effects play an important role in shaping the line width (27) and in dictating nonadiabatic dynamics (41). We measure the dephasing dynamics via the homogeneous line width extracted by means of 2D coherent excitation spectroscopy (34, 35). In our measurements, excitons generated coherently by a sequence of time-ordered and phase-matched femtosecond pulses scatter from incoherent background excitons and thereby undergo EID, which is perceived via changes of the homogeneous line width. We find that EID affects the complex lineshape by mixing absorptive and dispersive features in the real and imaginary spectral components; the real component of the 2D coherent spectrum initially displays a dispersive lineshape that evolves into an absorptive lineshape over the timescale at which EID couplings persist, and the imaginary component evolves in the converse fashion. Furthermore, we find that the homogeneous contribution to the spectral line width narrows with the population time, indicating a dynamic slowing down of the dephasing rate as the EID correlations active at early times dissipate. We find that the dynamic line narrowing phenomenon is reproduced by our stochastic scattering theory, which allows us to explore the effect of dynamic Coulomb screening on EID quantum dynamics.

2. NONLINEAR SPECTROSCOPIC SIGNATURES OF EID

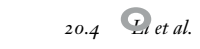
Two-dimensional coherent electronic spectroscopies are powerful techniques by which to identify and quantify many-body effects in semiconductors and they have been instrumental in the study of EID of excitons in 2D materials (21–24, 27, 37, 42). Much of the early work on semiconductor nanostructures was carried out by the Cundiff group (21–24), but here we focus on our recent work on a Ruddlesden–Popper metal halide, namely phenylethylammonium lead iodide [(PEA)₂PbI₄] (27, 37, 42), which is a 2D analog of a lead-iodide perovskite structure (see **Figure 1c**). We highlight the peculiar signatures of EID on the 2D exciton complex lineshape, the effect of exciton density on the homogeneous line width, and finally the time evolution of the spectral lineshape in Section 2.2, but first we briefly discuss the precedent set by Li and coworkers (22).

The early-time complex lineshape indicative of EID many-body correlations was previously observed in GaAs quantum wells (22). **Figure 3** displays the real part of the zero-population-time rephasing and nonrephasing spectra at excitation densities in which the signature of many-body interactions is clearly observed, and we identify a dispersive lineshape (derivative lineshape about the peak energy). This lineshape is in contrast to what is expected in the absence of many-body Coulomb contributions—the real lineshape is expected to be absorptive. We examine more extensively in Section 2.2 the effects that lead to this lineshape.

2.1. Optical Bloch Equations

The many-body exciton scattering signatures in the 2D coherent lineshape, shown in **Figure 3** for GaAs quantum wells, can be rationalized by numerical simulation based on modified OBEs (22). For a two-level system that includes both EID and excitation-induced shift (EIS) effects, the coherences carried by the off-diagonal term of the density matrix, ρ_{12} , evolve according to the following nonlinear OBE:

$$\dot{\rho}_{12} = -\left[(\gamma_0 + \gamma' N \rho_{22}) - i(\omega_0 + \omega' N \rho_{22}) \right] \rho_{12} + \frac{i}{\hbar} \mu_{12} \cdot \mathbf{E}(t) (\rho_{22} - \rho_{11})
= i \left[(\omega_0 + i\gamma_0) + (\omega' + i\gamma') N \rho_{22} \right] \rho_{12} + \frac{i}{\hbar} \mu_{12} \cdot \mathbf{E}(t) (\rho_{22} - \rho_{11}),$$
1.





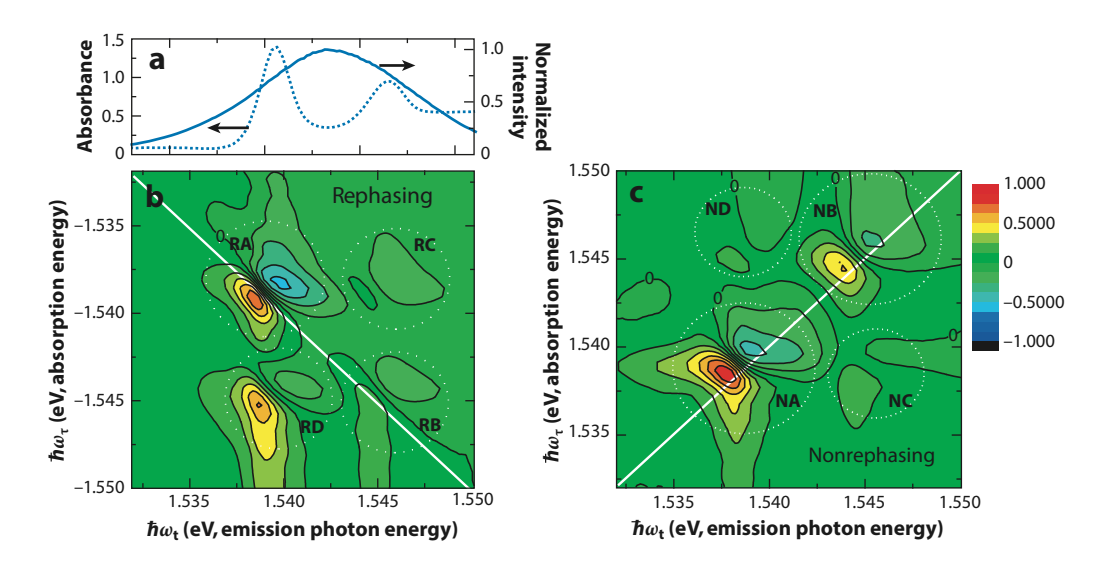


Figure 3

(a) Linear absorption, excitation pulse spectrum, and experimental real spectra for the (b) rephasing pulse sequences (RA–RD) and (c) nonrephasing pulse sequences (NA–ND) for GaAs quantum wells. Figure adapted with permission from Reference 22.

where γ_0 is the natural dephasing rate, ρ_{11} and ρ_{22} are the ground and excited state populations connected by coherence term ρ_{12} , N is the number density of chromophores, and γ' and ω' characterize the collision rate and collective interactions within the excited-state population. The last term corresponds to the driving field of the laser and dipole coupling between the ground and excited states. As the nonlinear OBE system evolves, both the total dephasing rate $[\gamma_0 + \gamma' N \rho_{22}(t)]$ and the phase oscillation frequency $[\omega_0 + \omega' N \rho_{22}(t)]$ depend on the fraction of chromophores in the excited state at time t. The evolution is nonlinear since the time evolution of $\rho_{22}(t)$ in principle depends on the coherence term when the laser is acting on the system. However, to a good approximation, $\rho_{22}(t)$ can be replaced with a simple exponential decay for times between pulses.

Figure 4 shows the predicted four-wave mixing signals for a two-level system with and without the term attributed to the EID component. Although the simple OBE approach does capture the narrowing, shift, and asymmetry of the lineshape, it fails to capture the phase scrambling that is clearly observed in the experimental signals in **Figure 3**. The real OBE signals are clearly absorptive rather than dispersive.

2.2. EID Effects in (PEA)₂PbI₄

As in GaAs quantum wells (**Figure 3**), EID effects are also observed in the complex 2D coherent excitation spectrum of (PEA)₂PbI₄. The linear absorption spectrum (**Figure 5**a) reveals a family of exciton polarons with binding energy offsets of ~40 meV (31, 38, 40); we label the dominant excitons as X_A and X_B and a shoulder at the blue edge of X_A as $X_{A'}$. We have previously reported that the multiple excitons identified in **Figure 5**a display strong many-body effects, manifested via the presence of stable biexcitons (39) and the dominance of EID signatures on the homogeneous line width (27). We have observed that X_A and X_B display different dependence of EID on the exciton density and on the temperature (27), and we have interpreted these phenomena as indicative of specific dynamic Coulomb screening of X_A and X_B by different polaronic dressing phonons (40).



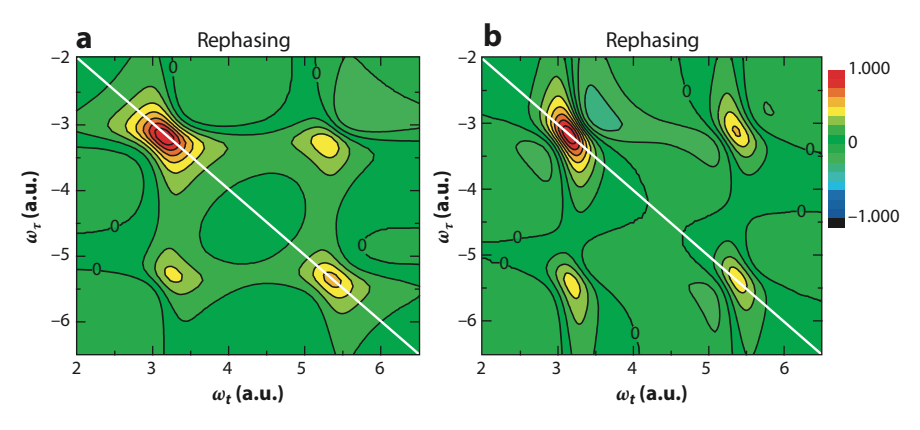


Figure 4

Calculated real spectra for the rephasing sequence. Panel *a* is based on a simple V system without any many-body interactions, while excitation-induced dephasing is included in panel *b*. Figure adapted with permission from Reference 22.

Figure 5*b,c* shows the real parts of two different coherent excitation pathways; the time ordering of the three optical pulses in the experiment and phase-matching conditions define the specific excitation pathways, based on which rephasing (**Figure 5***b*) and nonrephasing (**Figure 5***c*) spectra are obtained (43). In the rephasing experiment, the pulse sequence is such that the phase evolutions of the polarization after the first pulse and after the third pulse are of opposite signs, whereas in the nonrephasing experiment, they are of the same sign (see Equation 20; **Figure 2**) (cf 44). Both measurements shown in **Figure 5** are taken at a population waiting time of $\tau_p = 0$ fs

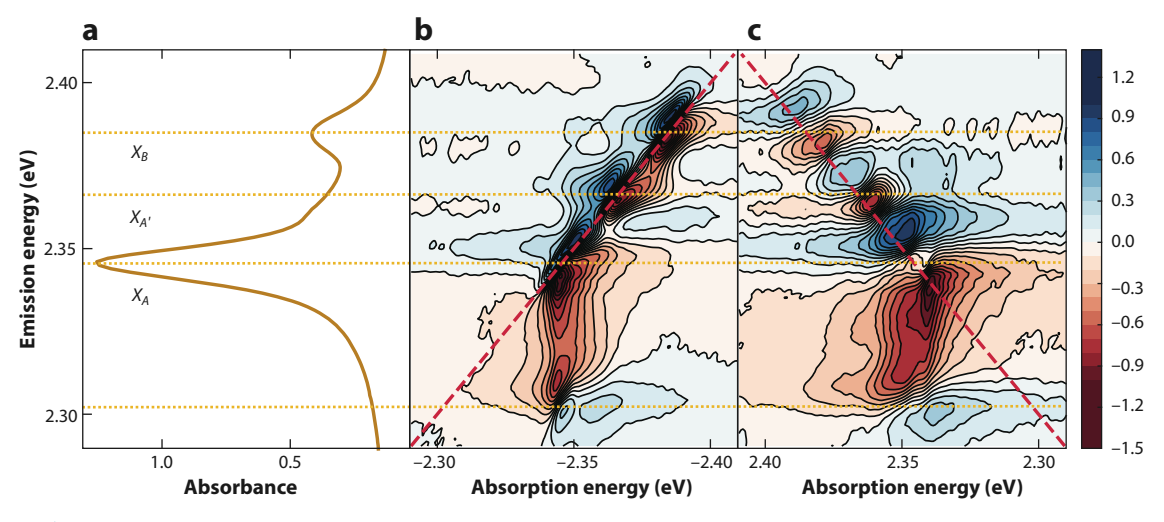


Figure 5

(a) Linear absorption spectrum of (PEA)₂PbI₄ at 5 K. Shown is the real part of the corresponding (b) rephasing and (c) nonrephasing spectra at a population time of $\tau_p = 0$ fs and at 5 K. The dotted orange lines connecting panels a–c indicate the positions of the three excitons in the linear absorption spectrum. The line at \sim 2.30 eV corresponds to a biexciton. The dashed red diagonal lines in panels b and c correspond to where the absorption energy equals the emission energy. The bar to the right of the figure displays the vertical false color scale in arbitrary units. Figure adapted with permission from Reference 37; copyright 2020 American Institute of Physics. Abbreviation: (PEA)₂PbI₄, phenylethylammonium lead iodide.



and an excitation fluence of 40 nJ/cm², which correspond to an exciton density in which we have identified effects of elastic exciton-exciton scattering (27). Corresponding diagonal spectral features at the energies of X_A , $X_{A'}$, and X_B (**Figure 5**) in both rephasing and nonrephasing spectra are observed. Apart from these diagonal peaks, we observe an off-diagonal excited-state absorption feature (opposite phase with respect to the diagonal features) corresponding to a correlation between the absorption energy of X_A and the emission energy of \sim 2.3 eV, which has no corresponding diagonal signal. We have assigned this cross-peak to a biexciton resonance (39). The full time series for the rephasing spectrum is in Reference 37 and reproduced in the **Supplemental Appendix**. From this, one can extract the homogeneous and inhomogeneous line widths via a global analysis of the diagonal and the antidiagonal lineshapes (34, 35).

 $τ_p$: time between pulses 2 and 3 in which the system is in a density-matrix population state, $|n\rangle\langle n|$

We now return to the complex zero-time spectral lineshape displayed in **Figure 5**. Upon close inspection, we notice that the real part of the spectrum displays a dispersive lineshape, i.e., derivative shape about the peak energy, for both diagonal and off-diagonal resonances, in both the rephasing and the nonrephasing spectra. Note the sign flip for the off-diagonal feature, which is consistent with its assignment to the excited-state absorption to the biexcitonic state (39). Similarly, the imaginary part of the spectra (given in the **Supplemental Appendix**) displays an absorptive lineshape. We have demonstrated that such dispersive lineshapes are a consequence of many-body correlations (37), consistent with the analysis of similar measurements in semiconductor quantum wells (22). These lineshapes are unexpected in the absence of many-body correlations; the real part of the spectrum should be absorptive and the imaginary part should be dispersive. The spectra in **Figure 5** therefore reveal phase mixing due to many-body Coulomb correlations responsible for EID.

To quantify the measured dynamic line narrowing, we display in **Figure 6** the homogeneous line width as extracted as in Reference 27 as a function of population time τ_p . By this analysis, **Figure 6** shows that the line width of X_A reduces most drastically but that the line width of X_B

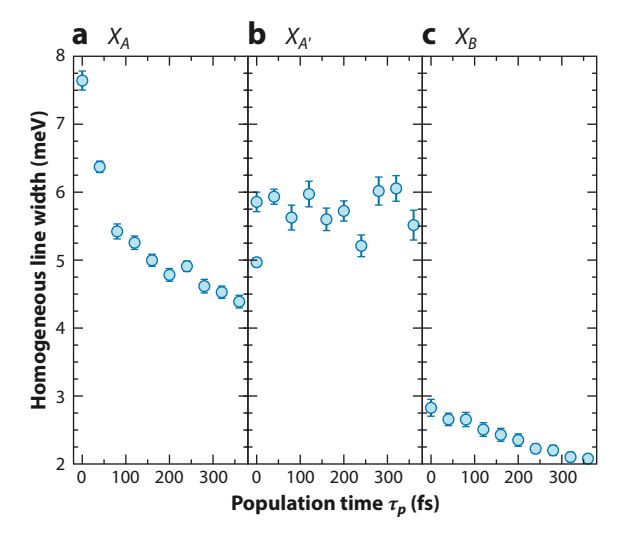


Figure 6

Homogeneous line widths obtained from the lineshape analysis of the absolute value of the rephasing spectra (see Reference 27) plotted as a function of the population time for (a) X_A , (b) $X_{A'}$, and (c) X_B exciton lines shown in **Figure 5**a. Figure adapted with permission from Reference 37; copyright 2020 American Institute of Physics.



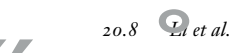
also reduces over a typical time window, whereas $X_{A'}$ displays no line narrowing. Previously, we (27) reported that X_A has a stronger density dependence on EID than X_B does, which is consistent with the observation derived from **Figure 6a,c**. We have found X_B to be more strongly displaced along phonon coordinates involving an octahedral twist in the plane of the inorganic layer and in the out-of-plane scissoring of the Pb-I-Pb apex (40). The stronger exciton-phonon coupling implies that X_B is more susceptible to dynamic screening than X_A is, which is consistent with the data in **Figure 6**. Finally, we point out that the asymptotic value of the homogeneous line width for X_A , $X_{A'}$, and X_B tends toward the low-exciton-density line widths that we reported in Reference 27.

The line width of $X_{A'}$ remains relatively constant over the probed population time. Although this might initially suggest that this resonance is immune to EID effects, we note that the real part of the rephasing spectrum associated with this particular transition exhibits a dispersive lineshape at all population times, consistent with the initial lineshapes of X_A and X_B . This lineshape indicates the clear presence of EID effects, as also confirmed by the density-dependent line width previously published in Reference 27. The trend shown in **Figure 6b**, on the other hand, suggests that the interexciton scattering does not evolve with the population time, at least within the probed time range. Inspection of the lineshape, however, suggests that the dispersive shape of the real part is preserved at all population times, implying that $X_{A'}$ is subjected to EID over a much longer period than the other two resonances. Following the arguments developed by the theoretical work described below, this dispersive lineshape implies the presence of a background exciton population that contributes to the scattering of $X_{A'}$ and whose stochastic evolution is that of the background of the other two resonances.

However, the decomposition of a 2D spectrum into its real and imaginary parts depends on the techniques applied, for example, through the comparison to an independent spectrally resolved differential transmission measurement. In other words, the feature of dispersive lineshape may be hidden in the imaginary part of the spectrum. On the other hand, from the Green's function approach, the EID and EIS are attributed, respectively, to the real and imaginary parts of the exciton self-energy renormalization. Therefore, the term of $\omega' + i \gamma'$ in Equation 1 cannot be treated separately in a quantum mechanical theory. As we illustrate later in our model, including the many-body interaction in the Hamiltonian leads to EID and the frequency shift effect in the spectral signals simultaneously.

What is then desired is an approach that incorporates the many-body dynamics of a dark, nonoptical population that coevolves with the optical signals. In this section, we accomplish this via the use of a stochastic lineshape approach, taken in the limit that the nonoptical population makes nonequilibrium and nonstationary contributions to the fluctuations of the optical energy gap.

In the next section, we present an overview of our recent work in developing spectroscopic models in which the energy gaps evolve in concert with a bath of background excitations that are both nonequilibrium and nonstationary as the result of being incoherently pumped by a series of laser pulses. Here, we develop the theory starting from a microscopic/many-body description of a system of excitons interacting via long-range Coulomb interactions and coupled to a dissipative environment. The theory is developed by deriving stochastic Langevin equations for the excitons and then using these derived spectral responses in the mean-field limit. The resulting model reduces to the well-known Anderson–Kubo model in the limit that the excitonic dynamics are stationary. The model provides a microscopic origin for the EID and EIS effects in semiconductor systems. As part of our review, we work through many of the technical details of the theory and our use of stochastic calculus to derive analytical expressions for the spectral responses.





3. NONLINEAR COHERENT SPECTROSCOPY OF NONSTATIONARY SYSTEMS

3.1. A Brief Review of Lineshape Theory

A spectroscopic measurement of a condensed-phase system interrogates both the system and its surrounding local environment. In the statistical sense, the background density of states coupled to the system being probed imparts an uncertainty in the energy of the transition. According to the Anderson-Kubo model (AK) (32, 33), this can be incorporated into the spectral response function by writing that the transition frequency has an intrinsic time dependence

$$\omega(t) = \omega_0 + \delta\omega(t), \qquad 2.$$

where ω_0 is the central (mean) transition frequency and $\delta\omega(t)$ is some time-dependent modulation with $\langle \delta \omega(t) \rangle = 0$. Lacking detailed knowledge of the environment, it is reasonable to write the frequency autocorrelation function in terms of the deviation about the mean, Δ , and a single correlation time, $\tau_c = \gamma^{-1}$, namely

$$\langle \delta \omega(t) \delta \omega(0) \rangle = \Delta^2 e^{-|t|/\tau_c}.$$

The model has two important limits (45). First, if $\Delta/\gamma \ll 1$, the absorption lineshape takes a Lorentzian functional form with a homogeneous width determined by the dephasing time T_2 $(\Delta^2/\gamma)^{-1}$. Second, if $\Delta/\gamma \gg 1$, the absorption spectrum takes a Gaussian form with a line width independent of the correlation time. In this limit, fluctuations are slow and the system samples a broad distribution of environmental motions. Increasing the rate of the fluctuations (i.e., decreasing the correlation time) leads to the effect of motional narrowing, whereby the line width becomes increasingly narrow (32, 33).

3.2. Stochastic Many-Body Processes

Our model is initiated by assuming that at t = 0 a nonstationary population of background excitations is created by a broadband laser excitation. This physical picture is sketched in Figure 1. In this review, excitation occurs with a sequence of phase-matched and time-ordered femtosecond pulses used to measure a coherent nonlinear excitation spectrum, and the excitons produced and measured via a well-defined coherent pathway (for the relevant excitons in this review, see Figure 2) are assumed to scatter elastically with their incoherent counterparts—excitons that are produced by the pulse sequence but have no phase relationship to those that produce signal in our experiments. The initial background population can be characterized by an average population N_0 and variance $\sigma_{N_0}^2$, both of which depend on the excitation pulse as well as the density of states of the material. Optical excitations at k=0 evolve in concert with a nonstationary ($k\neq 0$) background of excitations, in which the interaction is determined by a screened Coulomb potential, giving rise to a noisy driving term that effectively modulates the exciton energy gap.

Here, we consider the case where we have an ensemble of bosonic excitons described by a Hamiltonian written in second-quantized form as

$$H = \sum_{k} \hbar \omega_{k} a_{k}^{\dagger} a_{k} + \frac{1}{2} \sum_{kk',q} V_{q} a_{k+q}^{\dagger} a_{k'-q}^{\dagger} a_{k'} a_{k},$$

$$4.$$

where $V = L^3$ is the unit volume and V_a ,

$$V_q = \frac{1}{(2\pi)^3} \int V(\mathbf{r}) e^{-i\mathbf{q}\cdot\mathbf{r}} d\mathbf{r},$$
 5.

is the Fourier component of the many-body interaction potential. We now collect the $k \neq 0$ terms by keeping those interacting with k = 0 excitons and involving no more than two $k \neq 0$ states,

$$\begin{split} H &= \hbar \omega_0 a_0^{\dagger} a_0 + \sum_{q \neq 0} \hbar \omega_q a_q^{\dagger} a_q + \frac{V_0}{2} a_0^{\dagger} a_0^{\dagger} a_0 a_0 \\ &+ a_0^{\dagger} a_0 \left[2V_0 \sum_{q \neq 0} (a_q^{\dagger} a_q) \right] \\ &+ a_0^{\dagger} a_0^{\dagger} \left[\frac{V_0}{2} \sum_{q \neq 0} a_q a_{-q} \right] + a_0 a_0 \left[\frac{V_0}{2} \sum_{q \neq 0} a_q^{\dagger} a_{-q}^{\dagger} \right], \end{split}$$

and focus only the k = 0 term

$$H/\hbar = \omega_0 a_0^{\dagger} a_0 + \Omega \hat{A}^{\dagger} \hat{A}$$
$$+ \frac{\gamma_1}{2} \left(a_0^{\dagger} a_0^{\dagger} a_0 a_0 + 4 a_0^{\dagger} a_0 \hat{N} + a_0^{\dagger} a_0^{\dagger} \hat{A} \hat{A} + a_0 a_0 \hat{A}^{\dagger} \hat{A}^{\dagger} \right),$$
 7.

where the operators \hat{A} , \hat{A}^{\dagger} , and \hat{N} are collective bath operators defined by inspection of Equation 6. $\hbar \gamma_1 = V_0$ is the exciton-exciton interaction, which we obtain from the s-wave scattering length a and reduced mass μ within the Born approximation (46)

$$\gamma_1 = \frac{4\pi \, \hbar a}{\mu}.$$

This assumption does not rely upon the specific form of the exciton-exciton interaction, only that it be of finite range. In the current context, this interaction is due to Coulomb-mediated exciton-exciton scattering that gives rise to EID (27). However, it is possible that each distinct exciton within the family of the 2D perovskite system considered here (31) has a distinct and unique value of γ_1 , as we reported in Reference 27, where we demonstrated distinct Coulomb screening of different exciton polarons. For the purposes of our theoretical model, we assume that the system has a single exciton species that is susceptible to many-body scattering and therefore EID mediated via γ_1 .

3.3. Exciton Scattering Contributions in the Mean-Field (Hartree) Limit and Quantum Langevin Equations

The term involving \hat{N} introduces a mean-field interaction between the k=0 excitons and the net population of the $k \neq 0$ excitons. Consequently, it introduces energy fluctuation simply due to scattering of the $k \neq 0$ population from the k=0 population. The other two terms give rise to fluctuations/dissipation due to exciton pair creation/annihilation. For the moment, we neglect these terms but return to them in Section 3.5.

In the mean-field Hamiltonian equation (**Supplemental Equation B.4**), the background exciton population operator $\hat{N}(t) = \hat{A}^{\dagger}(t)\hat{A}(t)$ is of our interest. Using **Supplemental Equation B.11**, we deduce the Heisenberg equation of motion (for details and derivation, see the **Supplemental Appendix**).

For a stationary background population, i.e., $\langle N(t) \rangle = 0$, the population covariance evolves according to

$$\langle N(t)N(s)\rangle = \langle N(t-s)N(0)\rangle = \frac{\sigma^2}{2\Gamma} \exp(-\Gamma|t-s|).$$



In this limit, our model reduces to the Anderson–Kubo model in which the frequency fluctuates about a stationary average according to an Ornstein–Uhlenbeck process. In this case, the population relaxation time in our model is equivalent to the correlation time in the Anderson–Kubo model and this gives the rate at which the environment relaxes back to its stationary average given a small push. Moreover, the fluctuation amplitude, $\Delta\omega^2$, in the Anderson–Kubo model is equivalent to $\sigma^2/2\Gamma$ in our model. As we show, what appears at first to be a simple modification to the dynamics of a system has significant implications in terms of the nonlinear spectral response of the system.

Itô lemma: $(dW(t))^2 = dt$, where W(t) is the Wiener process

At time t=0, we push the background population significantly away from the steady-state distribution to an initial value of $\langle N(0)\rangle = N_0$, and the population evolves as

$$N(t) = N(0)e^{-\Gamma t} + \sigma \int_0^t e^{-\Gamma(t-s)} dW(s)$$
9.

and

$$\langle N(t)\rangle = e^{-\Gamma t} N_0, \tag{10}$$

where N_0 is the mean number of background excitations present at time t = 0.

In principle, there will be a distribution about this mean characterized by a variance $\sigma_{N_0}^2$. As a result, we break reversibility and the time symmetry of the correlation functions. Mathematically, this means that $\langle N(t)N(s)\rangle \neq \langle N(t-s)N(0)\rangle$ because the choice of initial time is no longer arbitrary.

In References 37 and 47 we used the Itô calculus to evaluate these correlation functions. From a practical point of view, the Itô calculus is a tool for manipulating stochastic processes that are closely related to Brownian motion and Itô lemma allows us to easily perform noise-averaged interactions. For the model at hand, the covariance of N(s) and N(t) is given by

$$Cov[N(s), N(t)] = \langle (N(s) - \langle N(s) \rangle)(N(t) - \langle N(t) \rangle) \rangle$$

$$= \frac{\sigma^2}{2\Gamma} \left[e^{-\Gamma|t-s|} - e^{-\Gamma(t+s)} \right] + \sigma_{N_0}^2 e^{-\Gamma(s+t)},$$
11.

with $\sigma_{N_0}^2$ being the variance of N(0). Similarly, the variance

$$Var[N(t)] = \left(\sigma_{N_0}^2 - \frac{\sigma^2}{2\Gamma}\right)e^{-2\Gamma t} + \frac{\sigma^2}{2\Gamma}$$
 12.

also depends on the initial fluctuation in the background population. Mathematically, the Fourier transform of the kernel of the integral in Equation 9 provides the spectral density of the noisy process. In fact, a trivial modification of the approach would be to replace the kernel in Equation 9 with another kernel reflecting a more complex spectral density. The resulting expressions for the responses are more complex indeed. However, Itô's lemma provides a tractable route for computing the necessary response functions.

3.4. Predictions from the Stochastic Model

Having established the mathematical model, let us briefly recapitulate some of its features. First, we started by assuming that the background population dynamics give rise to a stochastic process N(t) that enters into the Heisenberg equations of motion for the system operators. In particular, we assumed that N(t) corresponds to an overdamped Brownian oscillator and that at time t=0 there is a nonstationary population of background excitations. These two mathematical assumptions can be relaxed to some extent if one has a more detailed description of the spectral density of the background process and the initial background population. Second, we assume that averages



over exponential terms can be evaluated using the cumulant expansion. What then follows are the mathematical consequences as expressed in terms of the spectral responses of the model.

3.4.1. Linear response. The linear response for optical excitation is given by

$$S^{(1)}(t) = \frac{i}{\hbar} \langle \hat{\mu}(t) [\hat{\mu}(0), \rho(-\infty)] \rangle,$$
 13.

where $\hat{\mu}(t) = \mu(\hat{a}_0^{\dagger}(t) + \hat{a}_0(t))$ is the excitonic transition dipole operator and $\rho(-\infty)$ is the initial density matrix. The absorption spectrum is obtained by Fourier transformation.

Averaging over the fluctuations generates terms involving cumulants of the background noise, which result in terms such as

$$\left\langle \exp\left[i2\gamma_1 \int_0^t N(\tau) d\tau\right]\right\rangle \approx e^{i2\gamma_1 g_1(t) - 2\gamma_1^2 g_2(t)},$$
14.

where $\langle \cdot \cdot \cdot \rangle$ denotes averaging over noise. Note that the exciton interaction strength is $2\gamma_1$ in Equation B.4 of the **Supplemental Material**. Here, the first cumulant $g_1(t)$ gives rise to a characteristic frequency shift as the background population decays,

$$g_1(t) = \int_0^t \langle N(\tau) \rangle d\tau = \frac{N_0}{\Gamma} \left(1 - e^{-\Gamma t} \right),$$
 15.

and

$$g_{2}(t,t') = \int_{0}^{t} \int_{0}^{t'} \text{Cov}[N(\tau), N(\tau')] d\tau' d\tau$$

$$= \frac{\sigma^{2}}{2\Gamma^{3}} \left[2\Gamma \min(t,t') + 2e^{-\Gamma t} + 2e^{-\Gamma t'} - e^{-\Gamma |t'-t|} - e^{-\Gamma (t'+t)} - 2 \right]$$

$$+ \frac{\sigma_{N_{0}}^{2}}{\Gamma^{2}} \left[e^{-\Gamma (t+t')} - e^{-\Gamma t} - e^{-\Gamma t'} + 1 \right].$$
16.

When the two time limits are the same, this reduces to

$$g_{2}(t) = \int_{0}^{t} \int_{0}^{t} \text{Cov}[N(\tau), N(\tau')] d\tau d\tau'$$

$$= \frac{\sigma^{2}}{2\Gamma^{3}} \left(2\Gamma t + 4e^{-\Gamma t} - e^{-2\Gamma t} - 3 \right) + \frac{\sigma_{N_{0}}^{2}}{\Gamma^{2}} \left(1 - e^{-\Gamma t} \right)^{2}.$$
17.

In **Figure 7** we highlight some of the key physical effects that can appear in the linear absorption spectra based on our model. These effects are consistent with experimental observations and theoretical models of 2D semiconductors and TMDCs (27, 29, 39). **Figure 7**a displays the effect of a nonstationary background on the linear absorption spectrum of a system. The notable feature is the tail that extends to higher absorption energies. The character of this tail depends most strongly on the initial choice of N_0 and is attributable to the $g_1(t)$ term in our response function, which is the time integral over the evolving background population. This term, as it appears in Equation 13, produces an evolving frequency shift, reflecting the dynamic relaxation of the background. In the $S^{(1)}$ response, the background evolution is manifest as a tail extending out toward higher energies. A summary of the physical effects that can be attributed to the nonstationary evolution is given in the sidebar titled Spectral Effects That Can Be Attributed to the Nonstationary Evolution.

Figure 7*b* shows how the linear spectra are affected by the background relaxation rate γ for fixed values of $N_0 = 4$. In the case of fast background relaxation ($\Gamma = 50 \text{ meV}$), the exciton and biexciton splitting is clearly resolved and the lineshapes are Lorentzian about each peak. Decreasing



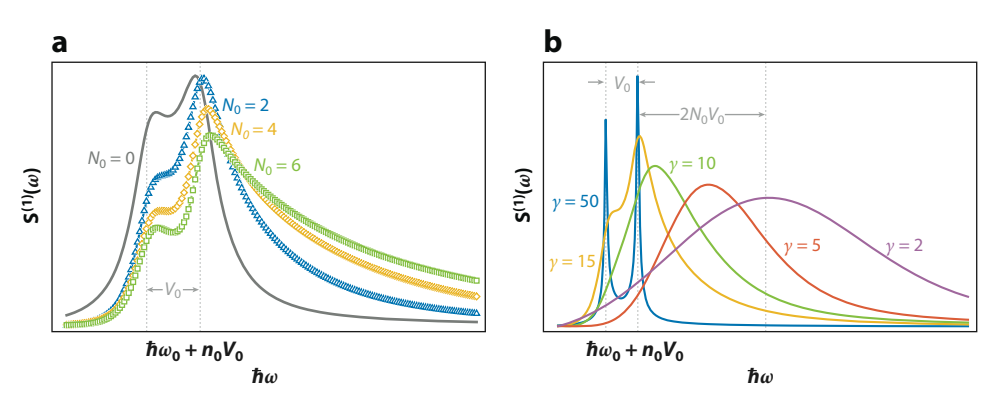


Figure 7

The linear response function with (a) increasing background population density N_0 , and (b) different relaxation rate Γ , from the homogeneous limit of $\Gamma=50$ meV to the inhomogeneous limit of $\Gamma=2$ meV. Figure reproduced from Reference 47.

the relaxation rate Γ produces a systematic shift toward the higher energies due to the mean-field interaction between the exciton and the background population. This shift saturates when the peak is fully shifted by $2V_0N_0$ and the spectral peak acquires a Gaussian form, reflecting mean N_0 and variance $\sigma_{N_0}^2$ of the initial background. In this slow-relaxation limit, the bright state is simply swamped and suppressed by the background excitation.

3.4.2. 2D coherent spectroscopy. In Reference 37 we discussed the linear response of our model and its relation to the Anderson–Kubo model. Here, we focus solely on the higher-order responses that reveal the dynamic evolution of the 2D coherent excitation lineshape. The third-order response involves phase-matched interactions of the system with a sequence of three laser pulses,

$$S^{(3)}(\tau_3, \tau_2, \tau_1) = \left(\frac{i}{\hbar}\right)^3 \langle \mu(\tau_3) [\mu(\tau_2), [\mu(\tau_1), [\mu(0), \rho(-\infty)]] \rangle.$$
 18.

SPECTRAL EFFECTS THAT CAN BE ATTRIBUTED TO THE NONSTATIONARY EVOLUTION

- 1. Blocking: Increasing the initial background exciton density suppresses the peak absorption intensity.
- 2. **Biexciton formation:** The peak is split by $\gamma_1/2$ corresponding biexciton interactions (39).
- 3. **(1D)** Energy shift: The peak position shifts toward higher energies with increasing background population due to increased Coulombic interactions.
- 4. **(1D) Broadening:** The spectrum acquires a long tail extending toward higher energies due to the dynamic evolution of the background.
- 5. **(2D) Phase scrambling:** This effect appears in the 2D coherent spectroscopy as an asymmetry along the absorption axis and as phase scrambling in the rephasing and nonrephasing signals.
- (2D) Excitation-induced shift: This systematic shift of peak position evolves as the background population decays.
- 7. **(2D)** Excitation-induced dephasing: Transient narrowing occurs along the off-diagonal due to the decreasing rate of exciton-exciton scattering.



The times $0 < \tau_1 < \tau_2 < \tau_3$ define the sequence of the time-ordered interactions in **Figure 2**. The expressions for the corresponding time correlation functions can be evaluated using the standard rules for double-sided Feynman diagrams (**Figure 2**) (cf 44), representing various optical paths that for a given pathway take the form

$$R_{\alpha}(\tau_{1}, \tau_{2}, \tau_{3}) = \left(\frac{i}{\hbar}\right)^{3} \mu^{4}(n_{0} + 1)^{2} \exp\left[i(\omega_{0} + n_{0}\gamma_{1})\sum_{j=1}^{3}(\pm)_{j}\tau_{j}\right] \left\langle \exp\left[i2\gamma_{1}\sum_{j=1}^{3}(\pm)_{j}\int_{0}^{\tau_{j}}N(s)ds\right]\right\rangle$$

$$= \left(\frac{i}{\hbar}\right)^{3} \mu^{4} (n_{0} + 1)^{2} \exp \left[i(\omega_{0} + n_{0}\gamma_{1}) \sum_{j=1}^{3} (\pm)_{j} \tau_{j}\right]$$

$$\times \exp \left[i2\gamma_{1} \sum_{j=1}^{3} (\pm)_{j} g_{1}(\tau_{j})\right] \exp \left[-2\gamma_{1}^{2} \sum_{i,j=1}^{3} (\pm)_{i} (\pm)_{j} g_{2}(\tau_{i}, \tau_{j})\right].$$
20.

The sign function $(\pm)_j$ takes + or - depending on whether the time step involves an excitation or a deexcitation of the system. The prefactor $(n_0 + 1)^2$ is for the pathways involving only the single-excitation manifold (distinguished by subscript a); it is $(n_0 + 1)(n_0 + 2)$ when double excitation (subscript b) is involved. **Figure 2** shows the most relevant diagrams for the rephasing and nonrephasing optical responses.

It is important to notice that the exciton-exciton interaction term γ_1 , and hence the screening due to exciton-lattice interactions, appears in three distinct places in the third-order responses: first, as a frequency shift due to self-interactions between the bright excitons; second, as a frequency shift due to interactions of bright excitons with the evolving background population density; and third, as the leading contribution to the lineshape. In addition, the third term involving $g_2(t)$ carries the influence of the initial conditions (via σ_{N_0}). The effect of many-body exciton-exciton scattering thus leads to time-evolving EID processes. Given these observations, we expect that the homogeneous line width will evolve with the population time, dictated by the evolution of $g_2(t)$.

Figure 8 and **9** correspond to the rephasing and nonrephasing behaviors of the theoretical model as parameterized to approximate the excitons in the 2D metal-halide perovskite system studied in the experimental investigations, which we describe later in this section. **Figure 8** gives the rephasing (**Figure 8**a,b) and nonrephasing (**Figure 8**c,d) spectra computed at $\tau_p = 0$. Two features highlighted above are immediately striking in the modeled 2D spectra. Both the asymmetry of the signals and the lineshape inversion of the real and imaginary spectral components can be traced specifically to terms within the response functions in Equation 20 that depend on the transient background relaxation and exciton self-interactions.

Both the phasing and the asymmetry evolve with increasing population time as shown in **Figure 9a–l.** Importantly, the real rephasing signal evolves from being dispersive at $\tau_p = 0$ to being absorptive at longer times. The imaginary rephasing signal (**Figure 9e–b**) has complementary phasing behavior, evolving from absorptive to dispersive. **Figure 9i–l** gives the absolute value of the total response as it evolves over τ_p . The peak is displaced from the diagonal, and its position as well as the line width evolves over τ_p .

In **Figure 9** we extract the contour corresponding to the half-maximum intensity at various indicated τ_p population times. Superimposed over each contour is one principal axis of the contour scaled according to its magnitude. The central points are the geometric centers of contours. This



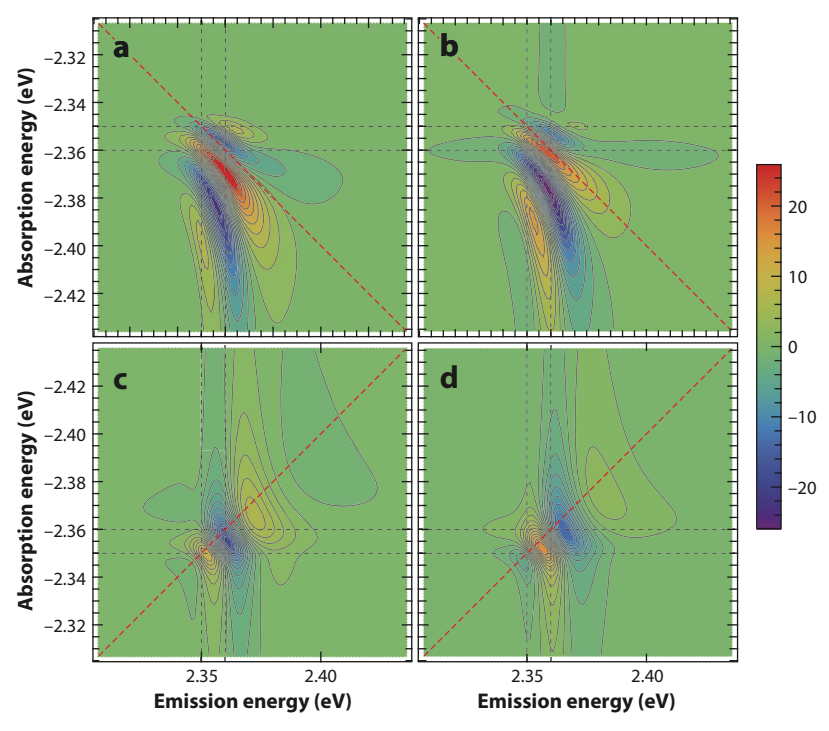


Figure 8

Theoretical real and imaginary spectra, respectively, of (a,b) rephasing and (c,d) nonrephasing phasematching and at population waiting time $\tau_p = 0$ fs. The two pairs of gray dashed lines correspond to the bare exciton energy at $\hbar\omega_0 = 2.35$ eV and the dressed exciton energy at $\hbar\omega_0 + \gamma_1 = 2.36$ eV.

analysis clearly shows that the peak systematically narrows, rotates, and distorts as the exciton coevolves with the background population. Moreover, the center peak shifts by about ~ 10 meV toward the red in both absorption and emission spectral dimensions as Coulombic interactions with the evolving background are diminished (10).

Within the stochastic model the frequency peak evolution is due to the first cumulant $g_1(\pm \tau_1, \pm \tau_2, \pm \tau_3)$, which introduced a phase shift that depends on the background population evolution as well as on the background displacements following each interaction with the laser field. The early-time blue shift and more rapid dephasing arise from many-body effects contained within g_1 . As the background population decays, the scattering effects are diminished. We note that if we set $g_1 = 0$ in Equation 20, the coherent response functions reduce to a stationary background, and the frequency peak evolution does not occur.

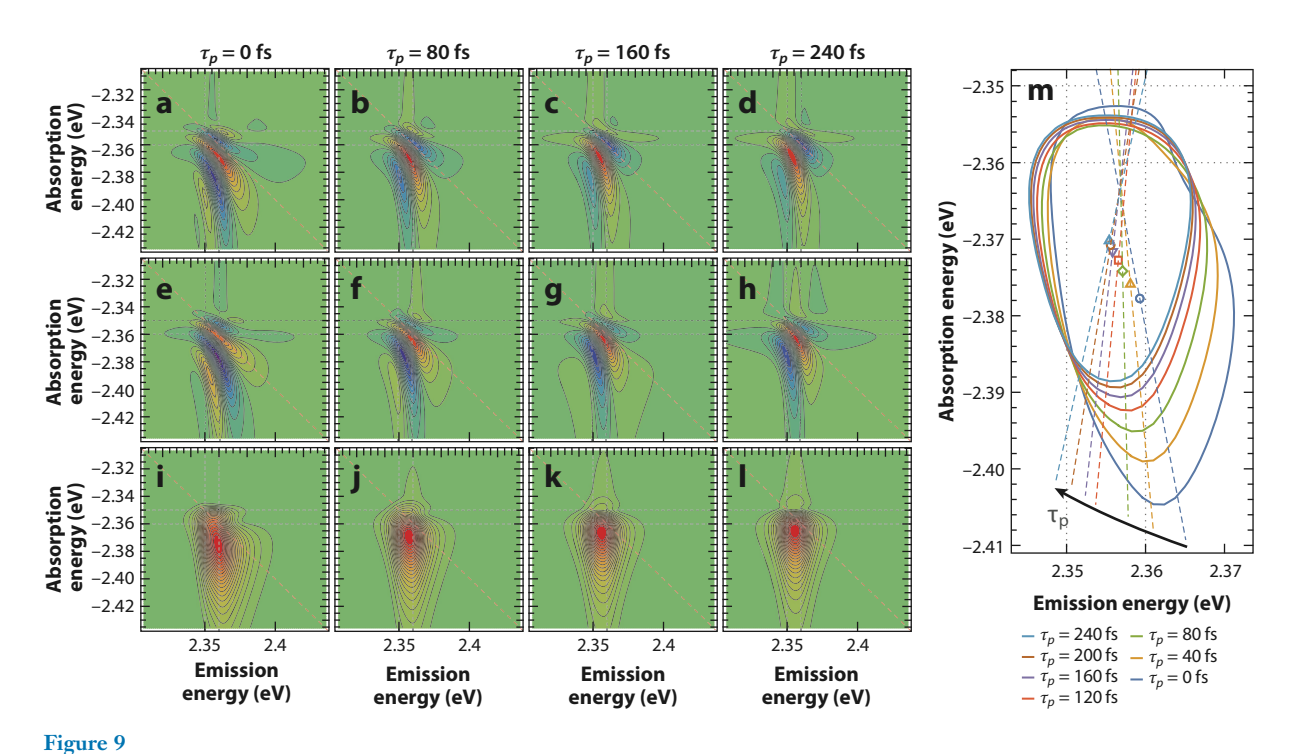
3.5. Exciton/Polaron Formation Dynamics due to Exchange Interactions

In deriving this model, we also assumed that an additional term corresponding to pair creation/annihilation could be dropped from consideration. That term takes the form

$$H_{\text{pair}} = \sum_{q \neq 0} \gamma_q (a_0^{\dagger} a_0^{\dagger} a_q^{\dagger} a_{-q} + a_q^{\dagger} a_{-q}^{\dagger} a_0 a_0)$$
 21.

and corresponds to the Boson exchange interaction, whereby momentum is transferred within the background population $(q \neq 0)$ as the result of interaction with the optical (q = 0) exciton.





(a–d) Real parts of theoretical rephasing spectra at population times τ_p indicated at the top of each panel. (e–b) Corresponding imaginary parts of the spectrum. (i–l) The norm (absolute value) of the optical response. The two pairs of gray dashed lines correspond to the bare exciton energy at $\hbar\omega_0 = 2.35$ eV and the dressed exciton energy at $\hbar\omega_0 + \gamma_1 = 2.36$ eV. (m) Exciton 2D coherent lineshape contour at half-maximum intensity as a function of the population waiting time derived from the theoretical rephasing absolute spectral evolution in **Figure 8**. The center of mass and one principal axis are shown for each contour.

However, such exchange terms may give important and interesting contributions to the spectral lineshape, especially in systems in which excitons are formed near the Fermi energy. In such systems, the exciton becomes dressed by virtual electron-hole fluctuations about the Fermi sea, producing spectral shifts and broadening the spectral lineshape. Such states are best described as excitons/polarons whose wave function consists of the bare exciton-hole excitation dressed by electron-hole fluctuations.

Ordinarily, as in the Bogoliubov treatment of Bose–Einstein condensates (48), one makes the semiclassical approximation that the condensate population can be taken as macroscopic, and as a result, one can replace the operators a_0 and a_0^{\dagger} with c-number $\sqrt{N_0}$. In our case, we continue to treat the background within the semiclassical limit and replace a_q and a_q^{\dagger} with $\sqrt{N_q}$ and write the coupling

$$\gamma(t) = \sum_{q \neq 0} N_q \gamma_q \approx \gamma_{\text{pair}} N(t),$$
 22.

where γ_{pair} is the exchange coupling constant and N(t) the net background population at time t.

To pursue the effect of the exciton/polaron formation, we start with the basic form of the Hamiltonian

$$H = \hbar\omega_0(a^{\dagger}a + 1/2) + \hbar\gamma(t)(a^{\dagger}a^{\dagger} + aa)/2,$$
 23.



where $\gamma(t)$ is the coupling, which we take to be an unspecified stochastic process. One can bring H into a diagonal form by unitary transformation

$$\tilde{H} = e^{-S} H e^{S} = \hbar \tilde{\omega}_0(t) \left(\tilde{a}^{\dagger} \tilde{a} + 1/2 \right), \tag{24}$$

with

$$\tilde{\omega}_0(t) = \sqrt{\omega_0^2 - \gamma(t)^2}.$$
 25.

However, because $\gamma(t)$ is a stochastic process, we need to use the Itô identity to properly derive the underlying stochastic differential equation (SDE) for the renormalized harmonic frequency, $\tilde{\omega}_0(t)$, in order to compute correlation functions.

In the regime of weak paired-excitation interaction, $\gamma/\omega_0 \ll 1$, the eigenfrequency can be approximated as

$$\tilde{\omega}_0(t) = \omega_0 \sqrt{1 - (\gamma/\omega_0)^2}$$

$$\approx \omega_0 (1 - z(t)/2),$$
26.

where $z(t) = \gamma(t)^2/\omega_0^2$. Therefore, \sqrt{z} represents the coupling strength of the paired excitations relative to the excitation frequency. For the moment, we leave the stochastic variable unspecified and find the linear response function

$$S^{(1)}(t) = \frac{i}{\hbar} \langle [\hat{\mu}(t), \hat{\mu}(0)] \rho(-\infty) \rangle$$

$$= \frac{i}{\hbar} \mu^{2} \langle [\tilde{a}^{\dagger}(t), \tilde{a}_{0}] \rho(-\infty) - \text{c.c} \rangle$$

$$= \frac{2\mu^{2}}{\hbar} \Im \left\{ \exp(i\omega_{0}t) \exp \left[-\frac{i\omega_{0}}{2} \int_{0}^{t} z(\tau) d\tau \right] \right\}$$

$$= \frac{2\mu^{2}}{\hbar} \Im \left\{ \exp(i\omega_{0}t) \exp \left[\sum_{n=1}^{\infty} \frac{(-i\omega_{0}/2)^{n}}{n!} \left\langle \left(\int_{0}^{t} z(\tau) d\tau \right)^{n} \right\rangle_{c} \right] \right\}$$
28.

in the form of cumulant expansion, where $\langle x^n \rangle \rangle_c$ denotes the *n*-th cumulant. According to the theorem of Marcinkiewicz (49, 50), the cumulant-generating function is a polynomial of degree no greater than 2 to maintain the positive definiteness of the probability distribution function. Therefore, we truncate the cumulant expansion to the second order and write the spectral lineshape functions $g_1(t)$ and $g_2(t)$ from the first cumulant and second cumulant,

$$g_1(t) = \int_0^t \langle z(\tau) \rangle d\tau$$
 29.

and

$$g_2(t) = \int_0^t \int_0^t \langle z(\tau), z(\tau') \rangle d\tau d\tau',$$
 30.

respectively.

We now make the simplifying assumption that $\gamma(t)$ satisfies the Ornstein–Uhlenbeck process, corresponding to vacuum fluctuations about bare exciton states,

$$d\gamma_t = -\theta \gamma_t dt + \sigma dW_t.$$
 31.

We should emphasize that this is not properly in the regime of quantum fluctuations, since we have not enforced the bosonic commutation relation within the background in making the semiclassical

//

www.annualreviews.org • Many-Body Exciton Scattering

20.17

Itô identity: if f(x(t)) is a function of a

stochastic variable with

dx = adt + bdW, then f satisfies the SDE:

df = f[x(t) + dx(t)]

-f[x(t)]

 $= (af' + \frac{1}{2}bf'')dt$



ansatz. This is clearly an avenue for future exploration. Applying the Itô identity, we arrive at an SDE for the exciton frequency,

$$dz_t = 2\theta \left(\frac{\sigma^2}{2\theta \omega_0^2} - z_t \right) dt + \frac{2\sigma}{\omega_0} \sqrt{z_t} dW_t,$$
32.

in which the relaxation rate is 2θ and the drift term $\sigma^2/2\theta\omega_0^2$ corresponds to the mean value of the stationary state. The formal solution, analogous to $\gamma(t)$ as the solution to the Ornstein–Uhlenbeck SDE, is

$$z(t)^{1/2} = [z(0)]^{1/2} e^{-\theta t} + \frac{\sigma}{\omega_0} \int_0^t e^{-\theta(t-s)} dW_s$$

$$\gamma(t) = \gamma(0)e^{-\theta t} + \sigma \int_0^t e^{-\theta(t-s)} dW_s.$$
33.

Using Itô isometry, we find the mean value

$$\langle z(t)\rangle = z_0 e^{-2\theta t} + \frac{\sigma^2}{2\omega_0^2 \theta} \left(1 - e^{-2\theta t}\right),$$
34.

and the correlation function

$$\langle z(t), z(s) \rangle = \sigma_{z_0}^2 e^{-2\theta(t+s)} + \frac{\sigma^4}{2\theta^2 \omega_0^4} \left[e^{-\theta|t-s|} - e^{-\theta(t+s)} \right]^2 + \frac{2\sigma^2}{\theta \omega_0^2} z_0 e^{-\theta(t+s)} \left[e^{-\theta|t-s|} - e^{-\theta(t+s)} \right], \quad 35.$$

which can be used to construct the g_1 and g_2 cumulants. Here, the initial distribution of z is determined by the mean $z_0 = \langle z(0) \rangle$ and the variance $\sigma_{z_0}^2 = \langle (z(0) - z_0)^2 \rangle$,

$$g_1(t) = \int_0^t \langle z(\tau) \rangle d\tau$$

$$= \frac{\sigma^2 t}{2\theta \omega_0^2} + \frac{1}{2\theta} \left(z_0 - \frac{\sigma^2}{2\theta \omega_0^2} \right) \left(1 - e^{-2\theta t} \right).$$
36.

The first cumulant of the model produces a red shift that is more complex than the counterpart in the simpler model, where interactions between paired excitations are neglected. The initial frequency shift $z_0\omega_0/2$ agrees with the Anderson–Kubo theory but converges to $\sigma^2/4\theta\omega_0$ rather than decaying to zero (see the sidebar titled Implications from the Exciton/Exciton Exchange Term). The first term can then be considered as a correction term that accounts for the interaction of exchange terms and leads to a constant red shift of $\sigma^2/4\theta\omega_0$.

IMPLICATIONS FROM THE EXCITON/EXCITON EXCHANGE TERM

- 1. The model produces the lineshape function given by the Anderson–Kubo model in the stationary limit, albeit with twice the coherence time.
- 2. The model captures the formation of exciton/polarons as the steady-state/long time limit and gives an exciton/polaron reorganization energy of $\sigma^2/4\theta\omega_0$, which reflects the coupling and spectral density of the background.



20.18 et al.

The second cumulant, $g_2(t)$, evaluates to

$$g_{2}(t) = \int_{0}^{t} \int_{0}^{t} \langle z(\tau), z(\tau') \rangle d\tau d\tau'$$

$$= \frac{\sigma_{z_{o}}^{2}}{4\theta^{2}} \left(1 - e^{-2\theta t} \right)^{2} + \frac{\sigma^{4}}{8\theta^{4} \omega_{0}^{4}} \left(e^{-4\theta t} + 8\theta t e^{-2\theta t} + 4e^{-2\theta t} + 4\theta t - 5 \right)$$

$$+ \frac{\sigma^{2}}{2\theta^{3} \omega_{0}^{2}} z_{0} \left(1 - 4\theta t e^{-2\theta t} - e^{-4\theta t} \right).$$
37.

If we compare this to the spectral function derived above,

$$g_2^{\text{EID}}(t) = \frac{\sigma_{\gamma_0}^2}{\theta^2} \left(1 - e^{-\theta t} \right)^2 + \frac{\sigma^2}{2\theta^3} \left(2\theta t + 4e^{-\theta t} - e^{-2\theta t} - 3 \right),$$
 38.

the first term is recovered; however, the present model provides a more sophisticated description of the dependency on the initial average z_0 . In the limiting case of the stationary state, where $\sigma_{\gamma_0}^2 = \sigma^2/2\theta$, the second cumulant in the present model turns into

$$g_2(t) = \frac{\sigma^4}{4\theta^4 \omega_0^4} \left(e^{-2\theta t} + 2\theta t - 1 \right) + \frac{\sigma^2 \gamma_0^2}{\theta^3 \omega_0^4} (e^{2\theta t} - 2\theta t - 1) e^{-2\theta t},$$
 39.

in which the first term reproduces the Anderson–Kubo lineshape but with half the correlation time $\tau_{\varepsilon} = (2\theta)^{-1}$ compared with that of the Anderson–Kubo theory θ^{-1} . Furthermore, the second term gives the line broadening due to the initial average of the background exciton population, γ_0^2 , which results only in a frequency shift in our previous model.

3.5.1. Contributions to 2D spectroscopy. The inhomogeneous and homogeneous contributions to the lineshape can be separated using 2D coherent spectroscopic methods (35, 42, 43, 51, 52). In most molecular applications of 2D spectroscopy, the evolving background plays little to no role in the spectral dynamics. However, the evolving background does affect the spectral lineshape by mixing absorptive and dispersive features in the real and imaginary spectral components. Generally speaking, systems lacking background dynamics exhibit absorptive lineshapes, and dispersive lineshapes are a consequence of many-body correlations (37), consistent with the analysis of similar measurements in semiconductor quantum wells (22). Furthermore, it is useful to compare the model presented here, which pertains to the exciton/exciton exchange coupling, with our previous model, which did not include this term and only considered the direct (Hartree) interaction. For this, we compute the third-order response $S^{(3)}$ under the impulsive/rotating-wave approximation. One easily finds that the responses for the various Liouville-space pathways take the form

$$R_{\alpha}(\tau_{3}, \tau_{2}, \tau_{1}) = \left(\frac{i}{\hbar}\right)^{3} \mu^{4} \left\langle \exp \left[i \sum_{j=1}^{3} (\pm)_{j} \int_{0}^{\tau_{j}} \tilde{\omega}_{0}(\tau) d\tau\right]\right\rangle, \tag{40}$$

where the angular brackets denote averaging over the stochastic noise term and the $(\pm)_j$ corresponds to whether the time step involves an excitation (+) or deexcitation (-) of the system. The time ordering of the three optical pulses in the experiment and phase-matching conditions define the specific excitation pathways, based on which photon echo $(k_s = -k_1 + k_2 + k_3)$ and virtual echo $(k_s = +k_1 - k_2 + k_3)$ signals can be obtained by heterodyne detection (the fourth pulse) (43). Equivalently, in the experiments using colinear phase-modulated pulses, rephasing $[-(\phi_{43} - \phi_{21})]$ and nonrephasing $[-(\phi_{43} + \phi_{21})]$ signals can be measured. In the rephasing experiment, the pulse

7

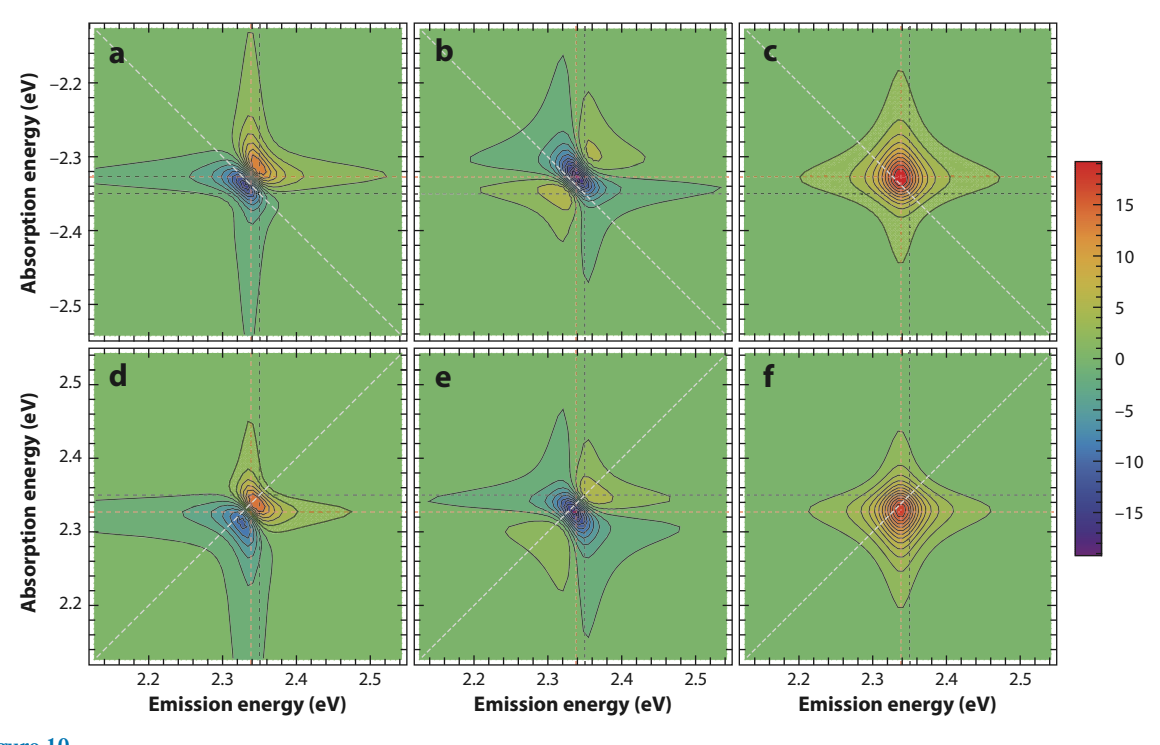


Figure 10
Rephasing (top) and nonrephasing (bottom) spectra at a population time of 100 fs based on the stochastic differential equation in Equation 31. Panels a and d are the real part, panels b and e are the imaginary part, and panels c and f are the norm of the spectra. The parameters used in the simulation are as follows: $\hbar\omega_0 = 2.35$ eV, $\sigma = 0.05$ fs^{-3/2}, $\theta = 0.01$ fs⁻¹, and $\gamma_0 = 0.5$ fs⁻¹. The black dashed lines mark the bare exciton energy $\hbar\omega_0$; the red dashed lines mark the shifts of $\omega_0 z_0/4 + \sigma^2/(8\theta\omega_0)$ and $-\sigma^2/(4\theta\omega_0)$ from ω_0 in the absorption and emission frequencies, respectively.

sequence is such that the phase evolution of the polarization after the first pulse and that after the third pulse are of opposite sign, while in the nonrephasing experiment, they are of the same sign. Equation 40 can be evaluated by cumulant expansion and the full expressions are given in the **Supplemental Appendix**. Because the $\tilde{\omega}_0(\tau)$ corresponds to a nonstationary process, the lineshape functions g_1 and g_2 contribute to the output signal.

Figure 10 presents the 2D rephasing and nonrephasing spectra corresponding to a single quantum state dressed by the paired-excitation terms. Focusing on the effect of interactions of paired excitations rather than on that of the initial condition, we set $\sigma_{\gamma_0}^2 = \sigma^2/(2\theta)$ so that the initial fluctuation is the same as that of the Wiener process (47). The initial distribution of z_0 is given by that of γ_0 :

$$\omega_0^2 z_0 = \sigma_{\gamma_0}^2 + \gamma_0^2, 41a.$$

$$\omega_0^4 \sigma_{z_0}^2 = 2\sigma_{\gamma_0}^4 + 4\sigma_{\gamma_0}^2 \gamma_0^2.$$
 41b.

The dispersive lineshape is observed in the real spectra for both rephasing and nonrephasing pulse sequences, which is a clear indication of the EID. The center of the peak deviates from the bare exciton energy $\hbar\omega_0=2.35$ eV due to the coupling between exciton pairs. Both the absorption and emission energies shift toward lower energies because z(t) is positive by definition (Equation 26). Although the Hamiltonian is diagonal after the exciton/polaron transformation using matrix S, the diagonal peaks are off the diagonal. Noting Equations 26 and 34, we find that



the emission frequency shifts from ω_0 by $-\sigma^2/(4\theta\omega_0)$, as long as the timescale of the experiment is greater than the relaxation time $(2\theta)^{-1}$. Indeed, this energy discrepancy attributed to the stationary state of z(t) can be considered as the exciton/polaron dressing energy. Regarding the absorption frequency measured by the first two pulses, because the system may not have sufficient time to relax, we can estimate from Equation 34 that the shift ranges between $\omega_0 z_0/2$ and $\sigma^2/(4\theta\omega_0)$. The median $\omega_0 z_0/4 + \sigma^2/(8\theta\omega_0)$ for absorption is shown.

3.5.2. Comparison to the Anderson–Kubo model. The well-known Anderson–Kubo theory describes the lineshape broadening with regard to the stationary state of a random variable (usually the frequency fluctuation, z_t here) characterized by an Ornstein-Uhlenbeck process. The expansion of the linear optical response function leads to the first cumulant $g_1^{AK}(t) = \beta t$, in which β is the drift term (i.e., the long-term mean value), and the second cumulant

$$g_2^{AK}(t) = \frac{\sigma^2}{2\theta^3} \left(e^{-\theta t} + \theta t - 1 \right).$$
 42.

In the short time limit $\theta t \ll 1$, the first cumulant in Equation 36 turns to $g_1(t) \approx z_0 t$, which has the same linear form as $g_1^{AK}(t)$. It also agrees with our previous model (see Equation 15 in Section 3.4.1) (37, 47),

$$g_1^{\rm EID}(t) = \frac{z_0}{2\theta} \left(1 - e^{-2\theta t} \right) \approx z_0 t. \tag{43}$$

Note that the relaxation rate here is 2θ instead of θ , because $\gamma(t)^2$, rather than $\gamma(t)$ characterized by the rate θ , is the stochastic process of interest. For the deterministic initial condition, we obtain $z_0 = \gamma_0^2/\omega_0^2$. The first cumulant $g_1(t)$ results in a red shift of $z_0\omega_0/2$ in the linear spectrum in the short time limit, which is determined by the initial average of the stochastic process z(t).

When the initial fluctuation of $\gamma(t)$ obeys the same Ornstein–Uhlenbeck process, we conclude that $\sigma_{\nu_0}^2 = \sigma^2/2\theta$ from the stationary state corresponding to the long time limit, where Equation 34 turns into $Var[\gamma(t)] = \sigma^2/2\theta$. Considering Equation 41a, we recast Equation 36 as

$$g_1(t) = \frac{\sigma^2}{2\theta\omega_0^2}t + \frac{\gamma_0^2}{2\theta\omega_0^2} (1 - e^{-2\theta t}),$$
44.

in which the second term looks similar to the $g_1^{\rm EID}(t)$ function in Equation 43. However, $z_0 =$ γ_0^2/ω_0^2 is true only for the deterministic initial condition, which is not the case in the above equation. Equation 43 given in our previous model leads to a time-dependent red shift that eventually vanishes after a sufficiently long time. The first term then can be considered as a correction term that accounts for the interaction of paired excitations and leads to a constant red shift of $\sigma^2/4\theta\omega_0$.

Therefore, the first cumulant of the present model produces the red shift similar to but more complex than the counterpart in our previous model, where interactions between paired excitations are neglected. The initial frequency shift $z_0\omega_0/2$ agrees with the Anderson-Kubo theory but converges to $\sigma^2/4\theta\omega_0$ rather than decaying to zero as in the previous model.

3.6. Inverting Spectral Lineshape to Obtain Underlying Dark State Dynamics

The practical utility of any spectroscopic method is to extract information about the system or sample being interrogated. However, any attempt to invert the physical signal depends on the model used for the input spectra and the model used to describe the coupling between the system and its environment. Here, we consider the case in which the lineshape function follows from the Anderson-Kubo model, but the underlying background process is due to the paired-fluctuation terms. In other words, the spectral fluctuations given by z(t) follow from an Ornstein–Uhlenbeck



process, but the underlying coupling is given by the transformed process $\gamma(t) = \omega_0 \sqrt{z(t)}$. Using the Itô lemma and integrating the resulting SDE, one has

$$\gamma(t) = \pm \omega_0 \sigma^{1/2} \left[\int_0^t e^{-\theta(t-\tau)} dW_\tau \right]^{1/2}$$
 45.

and uses this to construct the spectral density of the underlying many-body dynamics:

$$S(\Omega) = \int_{-\infty}^{+\infty} dt \langle \gamma_t \gamma_0 \rangle e^{-i\Omega t}.$$
 46.

However, since this involves taking averages over the Wiener process, we cannot directly use the Itô identity $dW_t^2 = dt$ to perform the integration. We can, however, find the upper limit of the covariance according to Jensen's inequality, which relates the value of a convex function of an integral to the integral of the convex function (53). Here, taking X as a random variable and φ as a convex function, Jensen's inequality gives

$$\phi(E[X]) \le E[\phi(X)]. \tag{47}$$

This is essentially a statement that the secant line of a convex function lies above the graph of the function itself. As a corollary, the inequality is reversed for a concave function such as \sqrt{x} . In cases of a stationary state or of $\gamma(0) = 0$, we have

$$\langle \gamma(t) \rangle \le \omega_0 \sigma^{1/2} \left(\int_0^t e^{-\theta(t-\tau)} dW_\tau \right)^{1/2} = 0,$$

$$48.$$

which indicates that $\langle \gamma(t) \rangle = 0$. The difference between the left and right sides of the inequality is termed the Jensen gap. Employing the inequality over a small integration range Δt , we obtain

$$\langle \gamma(t+\Delta t)\gamma(t)\rangle \leq \frac{\sigma\omega_0^2}{\sqrt{2\theta}}e^{-\theta|\Delta t|/2}.$$
 49.

This then implies a spectral density of

$$S(\Omega) = \int_{-\infty}^{+\infty} dt \langle \gamma_t \gamma_0 \rangle e^{-i\Omega t} \le \frac{2\sqrt{2\theta}\sigma\omega_0^2}{\theta^2 + \Omega^2}.$$
 50.

that can be well approximated by a Lorentzian in the limit that the Jensen inequality becomes an equality. Since the Lorentzian spectral density implies an underlying Ornstein-Uhlenbeck process for γ_t , in this limit the two cases considered here become identical. The equality is satisfied only when the convex (or concave) function is nearly linear over the entire given range of integration, which implies that $\theta \Delta t \gg 1$ in Equation 50, corresponding to homogeneous or lifetime limited broadening. We must also conclude that the Jensen inequality can be applied only in one direction, since starting from the assumption that γ_t is a mean-reverting Ornstein–Uhlenbeck process gives the results presented in Section 3.5. The curious observation then is that the lineshape for the more complex process appears to be bound by the Lorentzian form; that is, it must be more narrow than what one expects for exponential decay.

If we specify the initial value of the coupling $\gamma(0)$ at t = 0, we can use Jensen's inequality to compute an upper limit of the covariance as

$$\langle \gamma(t), \gamma(s) \rangle \leq \frac{\sigma \omega_0^2}{\sqrt{2\theta}} \left[e^{-\theta|t-s|} - e^{-\theta(t+s)} \right]^{\frac{1}{2}}.$$
 51.

If we take both t and s at some later times so that the memory of the initial condition is lost and take $\Delta t = t - s$, we recover Equation 49 as the stationary covariance.

In the nonstationary limit, however, the time evolution of the mean [and hence $g_1(t)$] is very different. Using Mathematica, we were able to arrive at an analytical expression for $\langle \gamma(t) \rangle$. Unlike its counterpart in Section 3.5, it does not relax exponentially to a stationary value and the resulting



long time value is far more complex. This suggests that one needs to look at both the lineshape and its temporal evolution to correctly extract the background dynamics.

4. PERSPECTIVE

Stochastic models have a long and important history in the field of chemical physics because they allow one to incorporate a trajectory-based viewpoint directly into the dynamics. The Anderson-Kubo model was an early attempt at providing a physical rationalization of how frequency fluctuations contribute to the absorption and emission lineshapes of molecules in contact with a thermal environment (32, 33, 54). The models have been continuously improved upon over the years, notably including more detailed descriptions of the bath and the actual coupling mechanisms between the system and the environment that lead to the frequency fluctuations (44, 55–58). As we have repeatedly pointed out, such approaches assume that the environment is in a stationary (e.g., thermal) state at time t = 0 and does not interact with any external stimulus over the course of the dynamics of the system. We argue here that in many cases one cannot ignore the fact that the broadband excitation pulses used in contemporary ultrafast experiments can create a background gas of excitons that can interact with an optical bright state, leading to fluency-dependent dynamics that can be manifest in terms of spectral shifts and tails even in linear absorption spectra. We conclude that these details can be further revealed through 2D coherent spectroscopy, especially when paired with a theoretical approach that accounts for the nonstationary evolution of the background.

Here, we have reviewed our approach based on a stochastic many-body treatment of the background and have provided several principal results and some technical details of our theoretical models. Throughout, we have used the Itô calculus when integrating over stochastic variables. This mathematical method provides us with a powerful avenue for obtaining analytical expressions for the various cumulants and correlation functions needed to compute the spectral responses. Fortunately, the current release of Mathematica (version 10 or higher) has a powerful stochastic calculus module that can be harnessed to evaluate both formally and numerically the cumulants and correlation functions for simple and complex transformed processes. Work remains to extend the approach toward both fermionic baths and strongly quantized baths such as those encountered in cavity quantum electrodynamics systems.

DISCLOSURE STATEMENT

The authors are not aware of any affiliations, memberships, funding, or financial holdings that might be perceived as affecting the objectivity of this review.

ACKNOWLEDGMENTS

The work at the University of Houston was funded in part by the National Science Foundation (CHE-2102506) and the Robert A. Welch Foundation (E-1337). The work at Los Alamos National Laboratory was funded by the Laboratory Directed Research and Development program (20220047DR). The work at the Georgia Institute of Technology was funded by the National Science Foundation (DMR-1904293).

LITERATURE CITED

- Mysyrowicz A, Grun J, Levy R, Bivas A, Nikitine S. 1968. Excitonic molecule in CuC1. Phys. Lett. A 26(12):615–16
- Magde D, Mahr H. 1970. Exciton-exciton interaction in CdS, CdSe, and ZnO. Phys. Rev. Lett. 24(16):890– 93







- Grun J, Nikitine S, Bivas A, Levy R. 1970. Luminescence of copper halides excited by a high power laser. *J. Lumin.* 1:241–53
- Miller R, Kleinman D, Gossard A, Munteanu O. 1982. Biexcitons in GaAs quantum wells. Phys. Rev. B 25(10):6545–47
- Kleinman D. 1983. Binding energy of biexcitons and bound excitons in quantum wells. Phys. Rev. B 28(2):871–79
- Hu Y, Koch SW, Lindberg M, Peyghambarian N, Pollock E, Abraham FF. 1990. Biexcitons in semiconductor quantum dots. Phys. Rev. Lett. 64(15):1805–7
- Brunner K, Abstreiter G, Böhm G, Tränkle G, Weimann G. 1994. Sharp-line photoluminescence and two-photon absorption of zero-dimensional biexcitons in a GaAs/AlGaAs structure. *Phys. Rev. Lett.* 73(8):1138–41
- 8. Albrecht T, Bott K, Meier T, Schulze A, Koch M, et al. 1996. Disorder mediated biexcitonic beats in semiconductor quantum wells. *Phys. Rev. B* 54(7):4436–39
- Stone KW, Gundogdu K, Turner DB, Li X, Cundiff ST, Nelson KA. 2009. Two-quantum 2D FT electronic spectroscopy of biexcitons in GaAs quantum wells. Science 324(5931):1169–73
- Karaiskaj D, Bristow AD, Yang L, Dai X, Mirin RP, et al. 2010. Two-quantum many-body coherences in two-dimensional Fourier-transform spectra of exciton resonances in semiconductor quantum wells. *Phys. Rev. Lett.* 104(11):117401
- Turner DB, Nelson KA. 2010. Coherent measurements of high-order electronic correlations in quantum wells. Nature 466(7310):1089–92
- Schultheis L, Kuhl J, Honold A, Tu CW. 1986. Ultrafast phase relaxation of excitons via exciton-exciton and exciton-electron collisions. *Phys. Rev. Lett.* 57(13):1635–38
- Honold A, Schultheis L, Kuhl J, Tu CW. 1989. Collision broadening of two-dimensional excitons in a GaAs single quantum well. Phys. Rev. B 40(9):6442–45
- Wang H, Ferrio K, Steel DG, Hu YZ, Binder R, Koch SW. 1993. Transient nonlinear optical response from excitation induced dephasing in GaAs. Phys. Rev. Lett. 71(8):1261–64
- Wang H, Ferrio KB, Steel DG, Berman PR, Hu YZ, et al. 1994. Transient four-wave-mixing line shapes: effects of excitation-induced dephasing. *Phys. Rev. A* 49(3):R1551–54
- Hu YZ, Binder R, Koch SW, Cundiff ST, Wang H, Steel DG. 1994. Excitation and polarization effects in semiconductor four-wave-mixing spectroscopy. *Phys. Rev. B* 49(20):14382–86
- Rappen T, Peter UG, Wegener M, Schäfer W. 1994. Polarization dependence of dephasing processes: a probe for many-body effects. Phys. Rev. B 49(15):10774–77
- Wagner HP, Schätz A, Maier R, Langbein W, Hvam JM. 1997. Coherent optical nonlinearities and phase relaxation of quasi-three-dimensional and quasi-two-dimensional excitons in ZnS_xSe_{1-x}/ZnSe structures. *Phys. Rev. B* 56(19):12581–88
- Wagner HP, Schätz A, Langbein W, Hvam JM, Smirl AL. 1999. Interaction-induced effects in the nonlinear coherent response of quantum-well excitons. *Phys. Rev. B* 60(7):4454–57
- Shacklette JM, Cundiff ST. 2002. Role of excitation-induced shift in the coherent optical response of semiconductors. Phys. Rev. B 66(4):045309
- Shacklette JM, Cundiff ST. 2003. Nonperturbative transient four-wave-mixing line shapes due to excitation-induced shift and excitation-induced dephasing. J. Opt. Soc. Am. B 20(4):764–69
- Li X, Zhang T, Borca CN, Cundiff ST. 2006. Many-body interactions in semiconductors probed by optical two-dimensional Fourier transform spectroscopy. *Phys. Rev. Lett.* 96(5):057406
- Moody G, Siemens ME, Bristow AD, Dai X, Karaiskaj D, et al. 2011. Exciton-exciton and exciton-phonon interactions in an interfacial GaAs quantum dot ensemble. *Phys. Rev. B* 83(11):115324
- Nardin G, Moody G, Singh R, Autry TM, Li H, et al. 2014. Coherent excitonic coupling in an asymmetric double InGaAs quantum well arises from many-body effects. Phys. Rev. Lett. 112(4):046402
- Moody G, Dass CK, Hao K, Chen CH, Li LJ, et al. 2015. Intrinsic homogeneous linewidth and broadening mechanisms of excitons in monolayer transition metal dichalcogenides. Nat. Commun. 6:8315
- Martin EW, Horng J, Ruth HG, Paik E, Wentzel MH, et al. 2018. Encapsulation narrows excitonic homogeneous linewidth of exfoliated MoSe₂ monolayer. arXiv:1810.09834 [cond-mat.mtrl-sci]





- 27. Thouin F, Cortecchia D, Petrozza A, Srimath Kandada AR, Silva C. 2019. Enhanced screening and spectral diversity in many-body elastic scattering of excitons in two-dimensional hybrid metal-halide perovskites. Phys. Rev. Res. 1:032032
- 28. Karki KJ, Widom JR, Seibt J, Moody I, Lonergan MC, et al. 2014. Coherent two-dimensional photocurrent spectroscopy in a PbS quantum dot photocell. Nat. Commun. 5(1):5869
- 29. Katsch F, Selig M, Knorr A. 2020. Exciton-scattering-induced dephasing in two-dimensional semiconductors. Phys. Rev. Lett. 124(25):257402
- 30. Erkensten D, Brem S, Malic E. 2020. Excitation-induced dephasing in 2D materials and van der Waals heterostructures. arXiv:2006.08392 [cond-mat.mtrl-sci]
- 31. Srimath Kandada AR, Silva C. 2020. Exciton polarons in two-dimensional hybrid metal-halide perovskites. J. Phys. Chem. Lett. 11(9):3173-84
- Anderson PW. 1954. A mathematical model for the narrowing of spectral lines by exchange or motion. J. Phys. Soc. Jpn. 9(3):316-39
- 33. Kubo R. 1954. Note on the stochastic theory of resonance absorption. 7. Phys. Soc. 7pn. 9(6):935-44
- 34. Siemens ME, Moody G, Li H, Bristow AD, Cundiff ST. 2010. Resonance lineshapes in two-dimensional Fourier transform spectroscopy. Opt. Express 18(17):17699-708
- 35. Bristow AD, Zhang T, Siemens ME, Cundiff ST, Mirin R. 2011. Separating homogeneous and inhomogeneous line widths of heavy- and light-hole excitons in weakly disordered semiconductor quantum wells. 7. Phys. Chem. B 115(18):5365-71
- 36. Li H, Piryatinski A, Srimath Kandada AR, Silva C, Bittner ER. 2019. Photon entanglement entropy as a probe of many-body correlations and fluctuations. 7. Chem. Phys. 150(18):184106
- 37. Srimath Kandada AR, Li H, Thouin F, Bittner ER, Silva C. 2020. Stochastic scattering theory for excitation-induced dephasing: time-dependent nonlinear coherent exciton lineshapes. J. Chem. Phys. 153(16):164706
- 38. Neutzner S, Thouin F, Cortecchia D, Petrozza A, Silva C, Srimath Kandada AR. 2018. Exciton-polaron spectral structures in two dimensional hybrid lead-halide perovskites. Phys. Rev. Mater. 2(6):064605
- 39. Thouin F, Neutzner S, Cortecchia D, Dragomir VA, Soci C, et al. 2018. Stable biexcitons in two-dimensional metal-halide perovskites with strong dynamic lattice disorder. Phys. Rev. Mater. 2(3):034001
- 40. Thouin F, Valverde-Chávez DA, Quarti C, Cortecchia D, Bargigia I, et al. 2019. Phonon coherences reveal the polaronic character of excitons in two-dimensional lead halide perovskites. Nat. Mater. 18:349-56
- 41. Thouin F, Srimath Kandada AR, Valverde-Chávez DA, Cortecchia D, Bargigia I, et al. 2019. Electronphonon couplings inherent in polarons drive exciton dynamics in two-dimensional metal-halide perovskites. Chem. Mater. 31:7085-91
- Srimath Kandada AR, Li H, Bittner ER, Silva-Acuña C. 2022. Homogeneous optical line widths in hybrid Ruddlesden-Popper metal halides can only be measured using nonlinear spectroscopy. J. Phys. Chem. C 126(12):5378-87
- 43. Cho M. 2008. Coherent two-dimensional optical spectroscopy. Chem. Rev. 108(4):1331–418
- 44. Mukamel S. 1995. Principles of Nonlinear Optics and Spectroscopy. Oxford, UK: Oxford Univ. Press
- 45. Hamm P, Zanni M. 2011. Concepts and Methods of 2D Infrared Spectroscopy. Cambridge, UK: Cambridge Univ. Press
- 46. Born M. 1926. Quantenmechanik der stoßvorgänge. Z. Phys. 38(11-12):803-27
- 47. Li H, Srimath Kandada AR, Silva C, Bittner ER. 2020. Stochastic scattering theory for excitation-induced dephasing: comparison to the Anderson-Kubo lineshape. J. Chem. Phys. 153(15):154115
- 48. de Gennes PG. 1999. Superconductivity of Metals and Alloys. Boca Raton, FL: CRC Press
- 49. Marcinkiewicz J. 1939. Sur une propriété de la loi de Gauß. Math. Z. 44(1):612-18
- 50. Rajagopal AK, Sudarshan ECG. 1974. Some generalizations of the Marcinkiewicz theorem and its implications to certain approximation schemes in many-particle physics. Phys. Rev. A 10(5):1852-57
- 51. Fuller FD, Ogilvie JP. 2015. Experimental implementations of two-dimensional Fourier transform electronic spectroscopy. Annu. Rev. Phys. Chem. 66:667–90
- 52. Tokmakoff A. 2000. Two-dimensional line shapes derived from coherent third-order nonlinear spectroscopy. 7. Phys. Chem. A 104(18):4247-55





- Jensen JLWV. 1906. Sur les fonctions convexes et les inégalités entre les valeurs moyennes. Acta Math. 30:175–93
- Kubo R. 1969. A stochastic theory of line shape. In Advances in Chemical Physics, ed. KE Shuler, pp. 101–27.
 New York: John Wiley & Sons
- 55. Reichman D, Silbey RJ, Suárez A. 1996. On the nonperturbative theory of pure dephasing in condensed phases at low temperatures. *J. Chem. Phys.* 105(23):10500–6
- Hsu D, Skinner JL. 1984. On the thermal broadening of zero-phonon impurity lines in absorption and fluorescence spectra. J. Chem. Phys. 81(4):1604–13
- 57. Skinner JL, Hsu D. 1986. Pure dephasing of a two-level system. J. Phys. Chem. 90(21):4931–38
- Mukamel S. 1985. Stochastic theory of resonance Raman line shapes of polyatomic molecules in condensed phases. J. Chem. Phys. 82:5398–408



